New Metrics for Industrial Depth Sensors Evaluation for Precise Robotic Applications*

Konrad P Cop[1,2], Arne Peters[1,2], Bare L Žagar[1,2], Daniel Hettegger[1] and Alois C Knoll[1]

Abstract— Precise perception is one of the key enablers of autonomous robotic operations. The right selection of sensors significantly influences the overall performance of the system. This paper provides a systematic approach for evaluation of various sensors available on the market. The main focus is to assess the performance in use cases of short to medium distance operations, especially relevant for precise manipulation and/or quality control. The evaluation is based solely on depth data (point clouds). We use six metrics to evaluate the sensors and propose a novel approach for low-cost fabrication of benchmark targets. The evaluation experiments are conducted on different materials to simulate various industrial environments. Our results provide a qualitative and quantitative comparison of different characteristics of various sensors and can be used to select an appropriate device for specific conditions.

I. INTRODUCTION

Recent years of advancements in sensor technology have grown a market of high-end industrial depth sensors which are advertised to reach sub-millimeter depth accuracy. However, the selection of the right sensor for a specific use-case can be quite hard, as their real-world performance heavily depends on the target environment, e.g. lighting conditions and/or surface materials. Comparing such sensors is a rather difficult task, as is creating a highly precise manufactured reference object or finding a reference sensor which is at least one magnitude more precise than the sensors accuracy.

As almost all recent benchmarks are focused on consumer-grade devices such as the Mircosoft Kinect or Intel Realsense families, we provide — to the authors' best knowledge — the first direct comparison featuring a wide selection of current, industrial grade depth sensors, suitable for precise, short to medium distance robotic applications. In detail, our contributions are:

1) We present a set of evaluation targets (see Fig. 1) that can be easily reproduced by using standard industrial components without relying on advanced manufacturing techniques like a CNC milling machine.
2) We introduce new metrics which are based on the XYZ information only (point clouds) and provide a systematic approach for evaluation of sensors' capabilities for robotic short-distance applications.

[1]All authors were with the Department of Informatics, Technical University of Munich (TUM), Bolzmanstr. 3, 85748 Garching, Germany, while the work of this paper was conducted. kcop.wiel@gmail.com {arne.peters | bare.luka.zagar | daniel.hettegger}@tum.de, knoll@in.tum.de
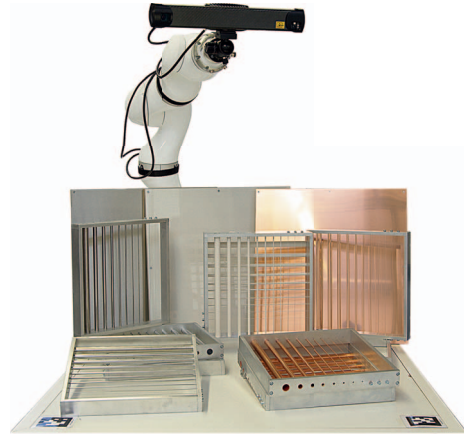[2]These authors contributed equally

Fig. 1. Evaluation targets and robot with attached Photoneo PhoXi sensor.

3) We perform a competitive evaluation of five state-of-the-art industrial, and three consumer-grade depth cameras.

Note that even though some of the featured sensors also record RGB data this benchmark only evaluates the provided 3D information.

II. RELATED WORK

Many metrics to evaluate the quality of point clouds have been proposed. Unfortunately most methods like point-to-point or point-to-plane distances, mean square error (MSE), Peak Signal to Noise Ratio (PSNR) [1], Hausdorff distance and Root mean square distance (RMSD) [2] rely on comparison to a known ground truth. Other approaches evaluate fused 3D data to rate the quality of scan alignments [3], [4] or the sensor's calibration [5]. Zhang et Al. proposed to use personal impressions of study participants to rate the quality of noisy point clouds [6]. An evaluation of objective and subjective comparison metrics can be found in [7].

Next to the comparison to known ground truths from a high precision sensor [8], [9], [10], [11], [12] and/or an accurately manufactured reference object [13], [14], three metrics have been widely used in the context of sensor benchmarking: 1) scanning of a known plane to analyze the sensor's z-accuracy and/or distortion [15], [11], [16], [17] as well as 2) recording a rectangular object to measure the edge noise (spatial precision in x and y direction) [15], [16], [17] and 3) analyzing the sensor's spatial resolution [15]. [16] further evaluates the sensor data depending on the view angle in an outdoor scene.

Most recent sensor benchmarks evaluated low cost consumer sensors and/or LiDARs, such as an actuated SICK

LMS-200 (ground truth), a SwissRanger SR-4000, a Fotonic B70 and a Microsoft Kinect camera [8], a Hokuyo URG-04LX, Hukuyo UTM-30LX and Sick LMS-151 [9], a Microsoft Kinect, ZESS MultiCam 3k and 19k, SoftKinetic DepthSense 311, PMD Technologies 3k-S and Camcube 41k [10], Kinect and Asus Xtion [13], Kinect II [16], [17], Microsoft Kinect II and Asus Xtion Pro [14], Intel Realsense SR300 [11], Intel Realsense D415 [12] and a comparison of ten different LiDARs for applications in Autonomouts driving [18]. One exception is the SET framework for the evaluation of stereo matching used to test a Stereolabs ZED and a Roboception rc_visard 160 [19]. Unfortunately, it is not applicable in our benchmark, as most of the included sensors obtain 3D information via *structured light* (SL) or *time of flight* (ToF).

III. EVALUATION METRICS

We use a total of six different metrics to evaluation the quality of tested depth sensors. Four of them, namely the *Z-Precision*, *Angle Dependent Reflectivity* (ADR), *Edge Precision* (EP) and *Spatial Resolution* (SR) have been widely used in the referred work. However, these metrics are computed on artificial scenes of flat surfaces. During experiments we realized that many sensors show better results on these kind of recordings than on real-world data. For example almost all tested sensors have some kind of integrated denoising filter on raw data, resulting in a high z-precision on planar surfaces. And, when it comes to actually measuring fine structures those tend to get filtered out. Simultaneously denoising techniques can also cause laser-shadow like artifacts, where smoothing on the edges of objects creates invalid z-values lying between fore- and background. As such, we propose two new metrics giving a better understanding of the sensors' behaviour on fine structures computed on scans of multiple cylindrical objects, aligned perpendicular to a sensor's view axis. The *Radius Reconstruction Accuracy* (RRA) evaluates a sensors capability of reconstructing curved surfaces, while the *Continuity* of a point cloud counts how many inliers of an object can be retrieved, depending on its diameter. These metrics show the smallest structures reliably measurable by a specific depth sensor.

In the definition of the following metrics we use

$$\mu(\boldsymbol{x}) = \frac{1}{N} \sum_{i=1}^{N} x_i \qquad (1)$$

and

$$\sigma(\boldsymbol{x}, \mu_x) = \sqrt{\frac{1}{N-1} \sum_{i=1}^{N} (x_i - \mu_x)^2} \qquad (2)$$

to express the mean and standard deviation of a vector $\boldsymbol{x}$ respectively. Each metric is computed on a scan of a specific object which is referred to as *target*. A detailed description of the used targets is given in section IV-B. Due to the dependency of the results on the surface reflectivity of the targets, we recommend to repeat the tests on different sets of materials.

A. Z Precision

The goal of this metric is to evaluate a sensor's depth precision, i.e. the dispersion of depth measurements. For calculating the depth precision we use a flat squared object of a known side length a as a target, which is aligned with the reference frame of the sensor. Precision is defined as the standard deviation of measurements to a known reference value [20] — in case of z the distances between the actual depth measurements and the target plane:

$$\zeta = \sigma(\boldsymbol{z}, \mu_z), \qquad (3)$$

where ζ is the precision, $\boldsymbol{z}$ the set of distances between the depth measurement values and the target plane, and μ_z the mean value of the distances between the depth measurements and the target plane.

B. Angle Dependent Reflectivity

As many depth sensors rely on a projection pattern their scan quality heavily depends on it being reflected back to the image sensor. Thus the ADR is based on the ratio of valid measurements n_{valid} obtained using a plane tilted by the angle ϕ with respect to the sensors view plane and the actual number of pixels n_{ideal} within this area q:

$$\alpha = \frac{n_{\text{valid}}}{n_{\text{ideal}}}. \qquad (4)$$

A measurement it considered as valid if it is not NaN and it's distance from the plane is below a multiple of ζ.

In case the target cannot cover a sensor's full field-of-view we propose to crop q to a fixed size square area with side length l_q, centered around the optical axis of a sensor, so that the number of visible measurement values remains the same for the entire range of tested angles between ϕ_{min} to ϕ_{max}. The length l_q is defined on a plane with $\phi = 0$ placed at a sensor's optimal working distance.
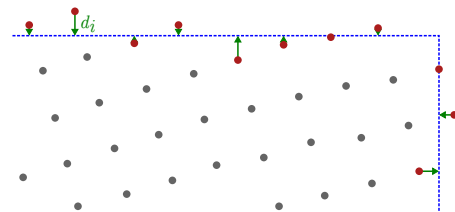
C. Edge Precision

Fig. 2. Schematic of the metric III-C evaluation procedure. Measured edge points of the target are coloured red, measured points which fall into the target, but aren't part the edge, are shown in gray and the blue dashed line represents the target edge lines. d_i corresponds to the i-th distance between a measured edge point and the target edge line.

While ζ estimates a sensors precision along its z axis, the EP is used to evaluate the overall lateral precision of a sensor in x and y direction. To evaluate the edge precision we again use a square shaped flat object of a known side length of l_q as a target. We calculate the standard deviation of the distance between each edge point and the target edge line, d_i depicted in Fig. 2.

In addition we introduce a condition that the minimum ratio of the number of registered edge points should be greater

than a threshold t_ϵ, as each sensor performs differently in terms of the amount of gaps in the measurements caused by e.g. reflections. The introduced ratio is defined by the ratio of the measured edge points m_ϵ^{edge} and ideal number of edge points $m_\epsilon^{\text{ideal}}$, which is derived from the spatial resolution.

$$\epsilon = \sigma(\boldsymbol{d}, \mu_d), \quad \text{if} \quad \frac{m_\epsilon^{\text{edge}}}{m_\epsilon^{\text{ideal}}} > t_\epsilon, \tag{5}$$

where ϵ is the edge precision, n_ϵ^{edge} is the number of measured points on the edge (red points in Fig. 2), $\boldsymbol{d}$ is the set of distances between each measurement along the edge, i.e. edge point, and the target edge line (green arrows) and μ_d is the mean of all distances between the measurements and the target edge. To ensure statistical correctness the target should be measured from multiple random poses.

D. Spatial Resolution

The SR ρ indicates the planar density of the sensor measurements (i.e. the number of points per cm^2) at a distance d, which is defined as:

$$\rho = {}^{n_\rho}/_A, \tag{6}$$

where n_ρ is the number of points and A the area. For the estimation of ρ we scanned a flat surface as a placed target orthogonal to the sensors optical axis and cut out the the registered points by a square shaped area with a known edge length of l_ρ. To achieve statistically correct results we repeat this calculation with multiple, randomly placed areas inside the measured flat surface.
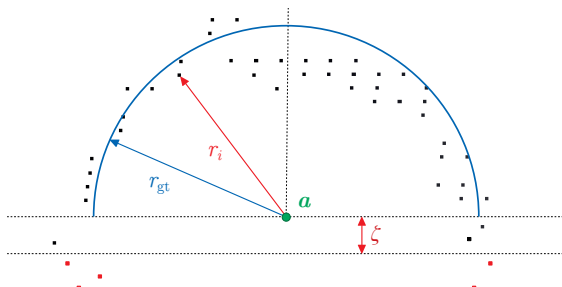
E. Radius Reconstruction Accuracy

Fig. 3.   RRA Parameters: r_{gt} is the expected radius of the target, r_i corresponds to the distance between each point and the axis $\boldsymbol{a}$ of the target. Due to the finite precision of the sensors one must also take into account the points that are located below the axis $\boldsymbol{a}$ but fall into the range of the z precision. Points considered in the metric are depicted in black while the ones disregarded - in red.

The RRA is used to evaluate a sensor's capability to reconstruct surfaces of different curvatures. The information used for evaluation is depicted in Fig. 3. For estimation, a cylindrical object with defined dimensions and position is used (e.g. a pipe or wire with known location). The points registered by the sensor should form a cylindrical shape p. For each point $\boldsymbol{p}_{p,i}$ in this point cloud $\boldsymbol{P}_p$ a distance $r_{p,i}$ is calculated. The calculations of all points are gathered into the mean radius $\mu_p = \mu(\boldsymbol{r}_p)$ and standard deviation σ_{p}. Depending on the sensor's edge precision and the material of the target, one might notice shadows on the edges of

the target. Since this is not the scope of this metric (this is covered by the EP in section III-C) we only include the points located in the upper half of the cylinder (blue line in Fig. 3). Additionally, due to the precision of the sensor, the points located under the axis $\boldsymbol{a}$, within the range of ζ, are also considered valid for the estimation, as those points result from a correct registration of the actual target, but their location might differ due to the z precision. To estimate the extremes of the reconstruction capabilities (the smallest measurable radius) we propose to use a set of various cylindrical objects (e.g. a target consisting of a set of pipes and/or wires as depicted in Fig. 5). Note that the cylinders should be solid in case a translucent material is being used. The numerical results of the metric are expressed for each cylinder p as:

- Difference between the (known) target radius $r_{p,\text{gt}}$ and estimated mean radius μ_p of $\boldsymbol{r}_p$:

$$\delta_p = |\, r_{p,\text{gt}} - \mu_p \,| \tag{7}$$

- Standard deviation of the calculated radii:

$$\sigma_p = \sigma(\boldsymbol{r}_p, \mu_{\text{p}}) \tag{8}$$

As the reconstruction precision can depend on the targets alignment towards a sensors baseline or projection pattern we propose to average the results of the RRA for multiple scans of the target in different orientations.
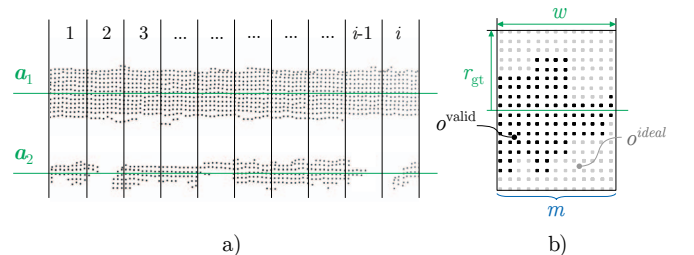
F. Point Cloud Continuity

Fig. 4.   a) An example of continuous point cloud (upper) and not completely continuous (bottom). $\boldsymbol{a}_1$ and $\boldsymbol{a}_2$ show the center axes of two cylinders. In case of the bottom cylinder, slices 2 and $i - 1$ are empty, resulting (in this case) in the continuity of 80%. b) Top view (projection) of a section of a cylinder representing a slice. r_{gt} is a radius of the target cylinder, w is the width of the slice. o_p^{valid} represents the registered points, o_p^{ideal} corresponds to the expected points estimated based on the spatial resolution. m refers to the theoretical expectation of a number of rows of points in the slice.

Depending on the reflectivity and angle of a material and dimensions of an object the registered point clouds might show inconsistency in density. This metric is tightly coupled to the previous one and both should be considered together for a valid evaluation of the sensor. For this reason we recommend to the same target as in the RRA. We propose to evaluate the continuity on a cylindrical object by dividing it into a set of *slices*, cut perpendicular to its center axis and classifying each as *empty* or *non-empty*. The sketch of the approach is depicted in Fig. 4 a). The overall continuity of the p-th cylinder is calculated as the ratio of the number of non-empty slices s_p^{ne} to the overall number of slices s_p:

$$\kappa_p = {}^{s_p^{\text{ne}}}/_{s_p} \tag{9}$$

TABLE I
SENSOR SPECIFICATIONS ACCORDING TO VENDORS

		Intel RealSense D415	Microsoft Kinect Azure	PMD CamBoard Pico Flexx	IDS Ensenso N35	Roboception rc_visard 65c	IDS Ensenso X36	Photoneo PhoXi 3D Scanner M	Zivid One Plus M
Sensor Technology		Active IR	ToF	ToF	SL	Active IR	SL	SL	SL
Acquisition Time [ms]		≥ 11.1	≥ 33.3	4.8 - 30	≥ 33.3	40 - 1 430	≥ 200	250 - 2 500	≥ 80
FOV [°]	H	65.0	75.0	62.0	62.8	61.0	46.7	48.8	33.0
	V	40.0	65.0	45.0	52.2	48.0	44.5	34.5	25.0
Range [mm]	Min	160	500	100	460	200	700	458	300
	Max	10 000	3 860	4 000	3 000	1 000	1 700	1 118	2 000
	Optimal	-	-	-	950	300 - 500	1 000	650	600 - 1 600
Color		Yes	Yes	-	No	Yes	No	No	Yes
Resolution [px]	Visual	1 920×1 080	3 840×2 160	-	1 280×1 024	1 280×960	2 448×2 048	2 064×1 544	1 920×1 200
	Depth	1 280× 720	640× 576	224×171	1 280×1 024	1 280×960	2 448×2 048	2 064×1 544	1 920×1 200
Scan Size [Points]		921 600	368 640	38 304	1 310 720	1 228 800	5 013 504	3 186 816	2 304 000
Baseline [mm]		55	32	16	100	65	400	350	137
Ext. Dims. [mm]	width	99	103	68	175	135	460	416	226
	height	23	39	17	50	96	65	77	86
	depth	20	125.4	7.35	52	75	80	68	165
Weight [g]		72	440	9	650	680	1 700	950	2 000
HW. Interface	Data	USB-C 3.1	USB-C 3.0	USB 2.0/3.0	Ethernet	Ethernet	Ethernet	Ethernet	USB-B 3.0
	Power	USB-C 3.1	USB	USB 2.0/3.0	12-24 V / PoE	18-30 V M12A	24 V	24 V-M12A / PoE	24 V-M12-5
Mounting		1/4"-20 UNC	1/4"-20 UNC	-	4 x M4	M3 / 1/4"-20 UNC	4 x M4	M4 / M8 / 3/8"-16 UNC	M6 / 1/4"-20 UNC
Price Range		Entry level	Entry level	Entry level	Medium	Medium	High-end	High-end	High-end

For consistent comparison across the sensors we propose a universal approach for defining slice sizes and classification of empty and non-empty slices. The length of the slice is based on the SR of the sensor (section III-D). For simplicity we assume that the points are distributed orderly in the point cloud and equally along x and y direction forming a square grid, while the size of the grid cell is sensor dependent. We define a slice as a section of the point cloud with a width of m points in the grid, as depicted in Fig. 4 b). The drawing shows the ideal points in case the sensor would return a valid depth value for every pixel on the target (grey) and the actual ones (black). The disproportion is caused by the combination of the material's reflectivity and the curvature of the object's surface. The theoretical number of points o_p^{ideal} depends on the SR, ρ and the dimensions of the slice (w and $r_{\text{p,gt}}$):

$$o_p^{\text{ideal}} = 2r_{p,gt} \cdot w \cdot \rho. \tag{10}$$

The slice is defined as non-empty if the ratio of the number of registered points o_p^{valid} is bigger than a threshold t, so that for a number of i slices we have:

$$s_p^{\text{ne}} = \sum_i \begin{cases} 1, & \frac{o_{p,i}^{\text{valid}}}{o_p^{\text{ideal}}} > t \\ 0, & \text{otherwise} \end{cases} \tag{11}$$

IV. EXPERIMENTAL SETUP

A. Tested Sensors

We used the metrics above to benchmark eight depth sensors from three different cost rages: 1) Intel RealSense D415 [21], 2) Microsoft Kinect Azure [22], 3) PMD Camboard pico flexx [23], 4) Ensenso N35-602-16-BL [24],

5) rc_visard 65c [25], 6) Ensenso X36-5CP-8/16/1000-400/1800 [26], 8) PhoXi 3D Scanner M [27] and 9) Zivid One+ M [28]. All key specifications of the sensors can be found in Table I. The tested rc_vizard 65c camera comes with an external random dot projector which has to be mounted on top of the camera and is not included in the given weight and dimensions. It is worth mentioning that the Intel RealSense D415, rc_visard 65c and PhoXi 3D Scanner M support on-board processing of raw data. Contrary, both Ensenso models as well as the Zivid One+ M are only supported by PCs with selected NVidia GPUs.

If possible we disabled all of the sensors integrated pre-processing functions.

B. Targets and Procedure

For the evaluation of the sensors by the z precision and ADR metrics flat square shaped targets were used depicted in Fig. 1. The targets consist of $50\,\text{cm} \times 50\,\text{cm}$ sheets and are fixed with screws to a $15\,\text{mm}$ thick wooden board to ensure flatness. For the z precision the targets were manually positioned in the center of the optical axis for each sensor to ensure best quality and scanned at nine different working distances $\pm 200\,\text{mm}$ around optimal distance with a step of $50\,\text{mm}$. Finally, for evaluation an optimal plane model was fitted to the registered point clouds and aligned with the reference frame. Afterwards the standard deviation ζ between the fitted plane and registered points was calculated.

For ADR we scanned the targets at 10 different angles from $0° - 45°$, with a step of $5°$, and with the target center placed at optimal distance. The side length of the cropped
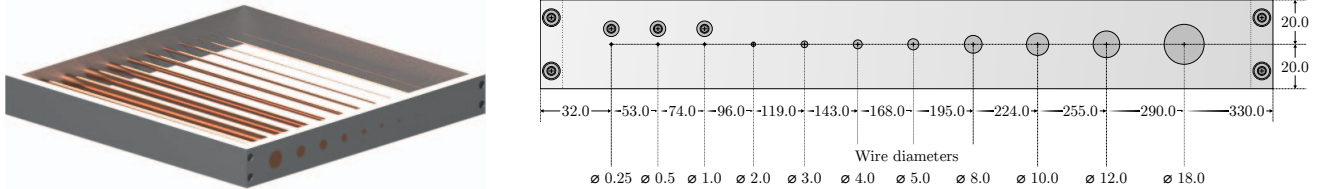
Fig. 5. Example of evaluation targets. For the experiments the same five materials of the cylinders were used as for the background. All measures are in mm. Wires of 1 mm diameter and below were wrapped around a screw on the outside of the frame to apply tension.

TABLE II
SPATIAL RESOLUTION ρ AND VISIBLE AREA AT OPTIMAL MEASURING DISTANCE

	Intel RealSense D415	Microsoft Kinect Azure	PMD CamBoard Pico Flexx	IDS Ensenso N35	Roboception rc_visard 65c	IDS Ensenso X36	Photoneo PhoXi 3D Scanner M	Zivid One Plus M
Measuring Distance [mm]	700*	750*	700*	950	600	1 000	650	800
Spatial Resolution [px/cm^2]	170	201	10	131	371	565	1 005	1 117
Visible Area [mm]	982×552	451×406	708×541	1 118×895	665×498	1 030×862	651×487	574×359

*For sensors without vendor specifications of the optimal measuring distance we used the smallest distance at which the target, used in metric III-E and III-F, was fully visible.
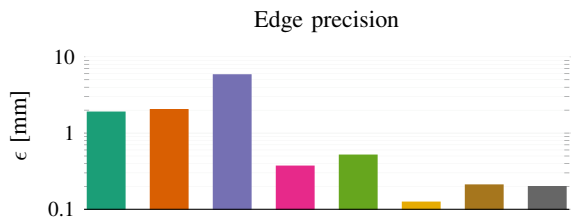

Fig. 6. Results of metric EP. Colors are the same as in Fig. 7.

square area was set to $l_q = 200$ mm. The points inside the cropped area define n_{valid} in Eq. 4.

To evaluate the sensors EP a square shaped flat matt steel sheet of $100 \times 100 \times 5$ mm was used and scanned at 10 random poses at each sensors individual optimal distance. The threshold for the minimum ratio of the number of edge points was set to $t_\epsilon > 50\%$. After extracting the target from the measurement data by using 3ζ as a parameter for plane fitting, the extracted target points were aligned with the mathematical model of the target. In order to ensure that all the points are registered by each sensor, a diffusely reflecting flat plastics surface was used to calculate the sensors SR which covered the entire scanning area of each sensor. The side length of the cropped area was set to $l_\rho = 100$ mm. To ensure statistical correctness over the entire field of view we repeated the procedure for ten random positions of the cropped area.

For the evaluation of the sensors with respect to RRA and continuity a set of targets as depicted in Fig. 5 was used. Note that the thinnest cylindrical object should not be detectable by any tested sensor in order to ensure each sensors measuring limits are determined. The targets were placed on different backgrounds to simulate different conditions, the resulting numerical outcomes were merged from different combinations of background materials and targets. The threshold for the percentage of points to consider a slice to be non-empty (Eq. 11) was set to $t = 50\%$ and the number

of rows for slice size to $m = 5$. For each sensor the target was placed in the optimal distance to ensure the best possible quality. To ensure proper estimation of reference axes, each point cloud was aligned with a ground truth point cloud (obtained from a CAD model) to allow proper estimation of the reference axes a_1 to a_{11}.

We used multiple sets of targets made of different materials, selected to demonstrate the limitations of current state-of-the-art depth sensors. As first tests indicated that matt materials — even when colored black — oppose very low difficulties to the sensors, we focused on more challenging reflective and/or transparent materials. We chose five materials, most commonly used in industry according to [29]: matt, natural POM plastics, brushed and polished stainless steel, copper and a combination of bars made of acrylic glass with optical fiber strings for the lower diameters. Plain sheets, bars/pipes and wires of all those materials can be bought precisely manufactured off the shelf, allowing easy reproduction of the targets.

We used an additional target composed of pipes of all used materials to configure the optimal exposure settings for each sensor. These settings, as well as the light conditions in our laboratory were kept constant during for all of following experiments

V. RESULTS

Our results of the z precision metric show how different materials influence the depth precision ζ of a sensor (Fig. 7). More reflective, i.e. shiny, materials decrease the depth precision. We did not include plots for our tests on acrylic glass, as all sensors looked right through it, retrieving either depth values of the scene's background or no data at all, thus making a detailed evaluation impossible.

In the results (Fig. 8) of metric ADP it is clearly depicted that with the increase of ϕ, the ratio α of scanned points
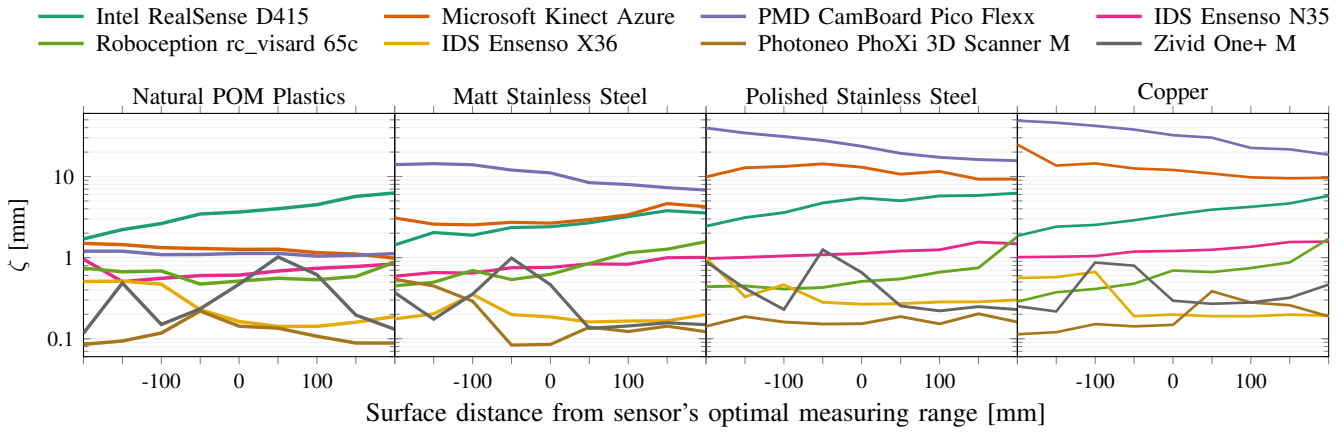
Fig. 7. Results of the z precision metric on four different materials.
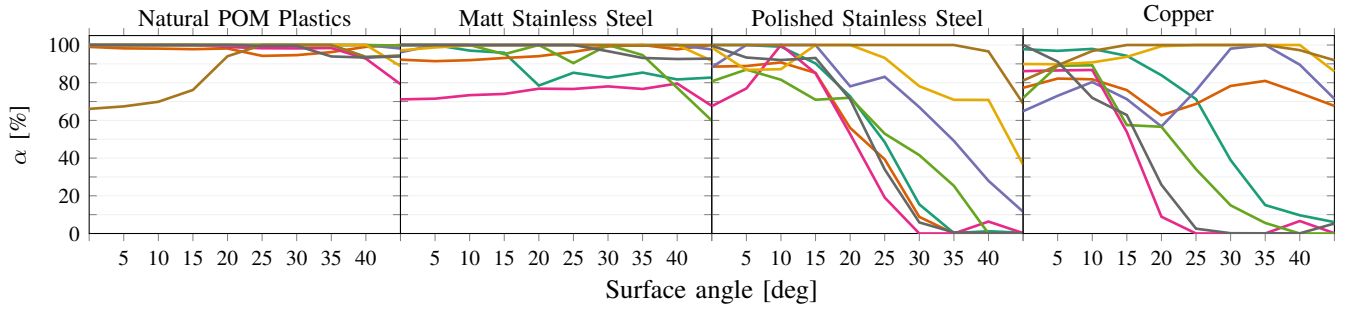

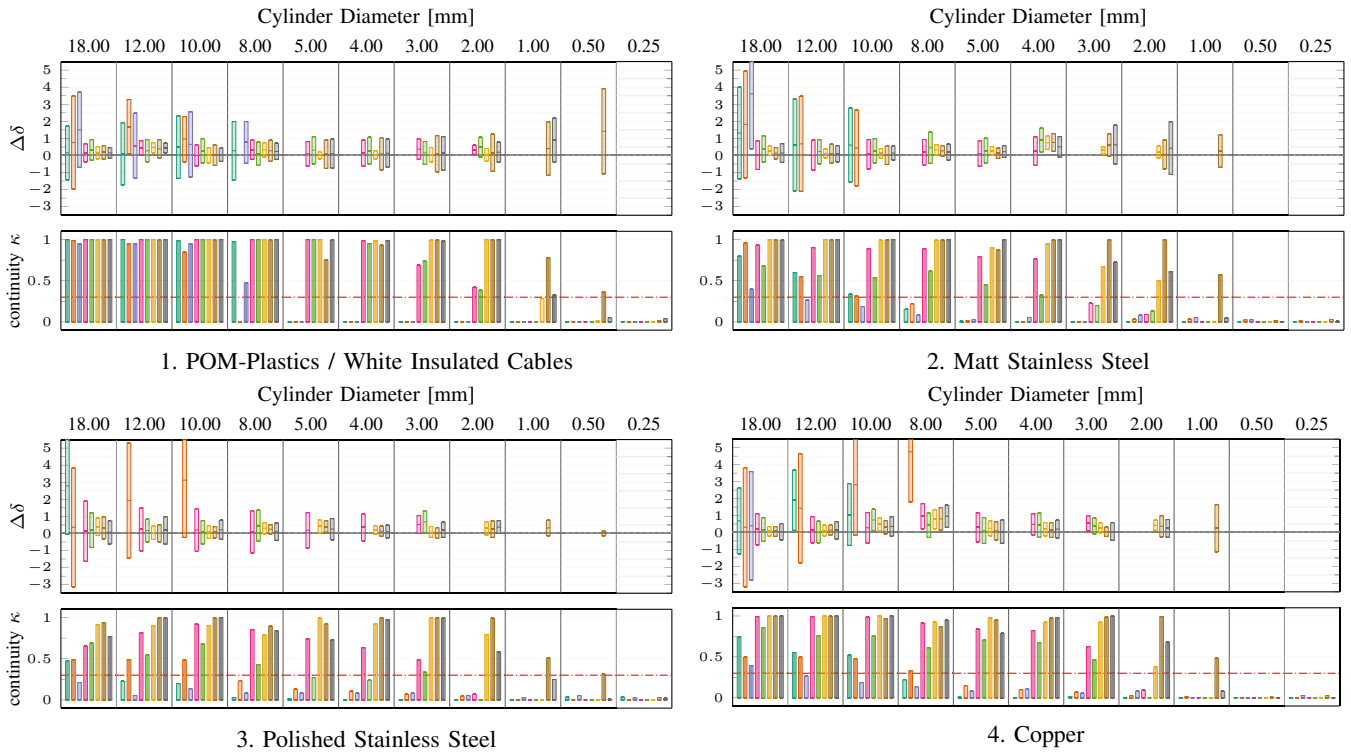Fig. 8. ADR on four different materials. Colors are the same as in Fig. 7.

Fig. 9. Results of RRA and continuity for different materials of the cylinder. In each case the top plot shows the results of RRA, the middle line of each bar corresponds to the estimated difference δ_p, while the bars represent the standard deviation of radius σ_p. The bottom plots shows the cylinder continuity. All colors are the same as in Fig 7. If the continuity drops below 30% (marked red), the corresponding radius results are not depicted as the noise influence is too high.

decreases. The decrease is even greater for more reflective surfaces.

Table II shows the density of each sensors measurements by SR at each sensor's optimal distance. The comparison of the results calculated with metric EP are depicted in Fig. 6. While the results of SR and EP are generally correlated the Ensenso X36 shows significantly better results than what we expected from its SR.

The results of the metrics RRA and continuity (Fig. 9) show that the minimum diameter of the objects that the sensors are able to detect is significantly larger than the actual z precision or SR of a sensor. Additionally, with the decrease of the pipes diameter both the δ_p and σ_p increase resulting in lower accuracy for tiny objects. It also becomes evident is that the continuity of registered point clouds highly depends on both the type of material and the diameter of the pipe. Again, the transparent targets made from acrylic glass were invisible to all sensors.

VI. CONCLUSIONS

This paper provided the evaluation of different depth sensors available on the market from various quality and cost ranges. With the introduced metrics we were able to perform quantitative and qualitative comparison of XYZ sensors' data and performance on different targets and materials. We believe the proposed metrics can be used in the future for the evaluation of other sensors and we expect the results to be relevant for selection of sensors for both industrial and scientific applications.

REFERENCES

[1] D. Tian, H. Ochimizu, C. Feng, R. Cohen, and A. Vetro, "Geometric distortion metrics for point cloud compression," in *2017 IEEE International Conference on Image Processing (ICIP)*. IEEE, 2017, pp. 3460–3464.

[2] A. Javaheri, C. Brites, F. Pereira, and J. Ascenso, "Subjective and objective quality evaluation of 3d point cloud denoising algorithms," in *2017 IEEE International Conference on Multimedia & Expo Workshops (ICMEW)*. IEEE, 2017, pp. 1–6.

[3] I. Bogoslavskyi and C. Stachniss, "Analyzing the quality of matched 3d point clouds of objects," in *2017 IEEE/RSJ International Conference on Intelligent Robots and Systems (IROS)*. IEEE, 2017, pp. 6685–6690.

[4] J. Chen, O. Mora, and K. Clarke, "Assessing the accuracy and precision of imperfect point clouds for 3d indoor mapping and modeling." *ISPRS Annals of Photogrammetry, Remote Sensing & Spatial Information Sciences*, vol. 4, 2018.

[5] M. Sheehan, A. Harrison, and P. Newman, "Automatic self-calibration of a full field-of-view 3d n-laser scanner," in *Experimental robotics*. Springer, 2014, pp. 165–178.

[6] J. Zhang, W. Huang, X. Zhu, and J.-N. Hwang, "A subjective quality evaluation for 3d point cloud models," in *2014 International Conference on Audio, Language and Image Processing*. IEEE, 2014, pp. 827–831.

[7] E. Alexiou and T. Ebrahimi, "On subjective and objective quality evaluation of point cloud geometry," in *2017 Ninth International Conference on Quality of Multimedia Experience (QoMEX)*. IEEE, 2017, pp. 1–3.

[8] T. Stoyanov, A. Louloudi, H. Andreasson, and A. J. Lilienthal, "Comparative evaluation of range sensor accuracy in indoor environments," in *5th European Conference on Mobile Robots, ECMR 2011, September 7-9, 2011, Örebro, Sweden*, 2011, pp. 19–24.

[9] F. Pomerleau, A. Breitenmoser, M. Liu, F. Colas, and R. Siegwart, "Noise characterization of depth sensors for surface inspections," in *2012 2nd International Conference on Applied Robotics for the Power Industry (CARPI)*. IEEE, 2012, pp. 16–21.

[10] B. Langmann, K. Hartmann, and O. Loffeld, "Increasing the accuracy of time-of-flight cameras for machine vision applications," *Computers in industry*, vol. 64, no. 9, pp. 1090–1098, 2013.

[11] M. Carfagni, R. Furferi, L. Governi, M. Servi, F. Uccheddu, and Y. Volpe, "On the performance of the intel sr300 depth camera: metrological and critical characterization," *IEEE Sensors Journal*, vol. 17, no. 14, pp. 4508–4519, 2017.

[12] M. Carfagni, R. Furferi, L. Governi, C. Santarelli, M. Servi, F. Uccheddu, and Y. Volpe, "Metrological and critical characterization of the intel d415 stereo depth camera," *Sensors*, vol. 19, no. 3, p. 489, 2019.

[13] H. Gonzalez-Jorge, B. Riveiro, E. Vazquez-Fernandez, J. Martínez-Sánchez, and P. Arias, "Metrological evaluation of microsoft kinect and asus xtion sensors," *Measurement*, vol. 46, no. 6, pp. 1800–1806, 2013.

[14] M. G. Diaz, F. Tombari, P. Rodriguez-Gonzalvez, and D. Gonzalez-Aguilera, "Analysis and evaluation between the first and the second generation of rgb-d sensors," *IEEE Sensors journal*, vol. 15, no. 11, pp. 6507–6516, 2015.

[15] M. R. Andersen, T. Jensen, P. Lisouski, A. K. Mortensen, M. K. Hansen, T. Gregersen, and P. Ahrendt, "Kinect depth sensor evaluation for computer vision applications," *Aarhus University*, pp. 1–37, 2012.

[16] P. Fankhauser, M. Bloesch, D. Rodriguez, R. Kaestner, M. Hutter, and R. Siegwart, "Kinect v2 for mobile robot navigation: Evaluation and modeling," in *2015 International Conference on Advanced Robotics (ICAR)*. IEEE, 2015, pp. 388–394.

[17] L. Yang, L. Zhang, H. Dong, A. Alelaiwi, and A. El Saddik, "Evaluating and improving the depth accuracy of kinect for windows v2," *IEEE Sensors Journal*, vol. 15, no. 8, pp. 4275–4285, 2015.

[18] J. Lambert, A. Carballo, A. M. Cano, P. Narksri, D. Wong, E. Takeuchi, and K. Takeda, "Performance analysis of 10 models of 3d lidars for automated driving," *IEEE Access*, vol. 8, pp. 131 699–131 722, 2020.

[19] N. F. Heide, A. Albrecht, and M. Heizmann, "Set: Stereo evaluation toolbox for combined performance assessment of camera systems, 3d reconstruction and visual slam," in *2019 IEEE 2nd International Conference on Information Communication and Signal Processing (ICICSP)*. IEEE, 2019, pp. 352–356.

[20] "Accuracy (trueness and precision) of measurement methods and results - Part 3: Intermediate measures of the precision of a standard measurement method," International Organization for Standardization, Geneva, CH, Standard, Dec. 1994.

[21] "Intel RealSense D400 Series Product Family," Intel Corporation, https://www.intel.com/content/dam/support/us/en/documents/emerging-technologies/intel-realsense-technology/Intel-RealSense-D400-Series-Datasheet.pdf, Tech. Rep., 5 2019, Accessed: 2020-10-30.

[22] "Azure Kinect DK hardware specifications," Microsoft Corporation, https://docs.microsoft.com/en-us/azure/Kinect-dk/hardware-specification, Tech. Rep., 2 2020, Accessed: 2020-10-30.

[23] "Camboard pico flexx," PMD Technologies AG, https://pmdtec.com/picofamily/wp-content/uploads/2018/03/PMD_DevKit_Brief_CB_pico_flexx_CE_V0218-1.pdf, Tech. Rep., 2018, Accessed: 2020-10-30.

[24] "N35-602-16-BL," IDS Imaging Development Systems GmbH, https://en.ids-imaging.com/ensensoprodukt.html?modelName=N35-602-16-BL, Tech. Rep., 10 2020, Accessed: 2020-10-30.

[25] "rc_visard," Roboception GmbH, https://doc.rc-visard.com/latest/pdf/rc_visard_manual_en.pdf, Tech. Rep., 10 2020, Accessed: 2020-10-30.

[26] "Ensenso X36 3D, 5MP, 8mm, Ext. 100," IDS Imaging Development Systems GmbH, https://en.ids-imaging.com/ensensoprodukt.html?modelName=X36-5CP-8%2F16%2F1000-400%2F1800, Tech. Rep., 10 2020, Accessed: 2020-10-30.

[27] "PhoXi 3D Scanner M," Photoneo s.r.o., https://photoneo.com/wp-content/uploads/datasheets/PhoXi3DScannerM-Datasheet-08_2020.pdf, Tech. Rep., 8 2020, Accessed: 2020-10-30.

[28] "Zivid One+ Technical specification," Zivid AS, https://www.zivid.com/hubfs/files/SPEC/Zivid%20One%20Plus%20Datasheet.pdf, Tech. Rep., 5 2019, Accessed: 2020-10-30.

[29] OECD, *Material Resources, Productivity and the Environment*, 2015.